Document downloaded from:

http://hdl.handle.net/10251/176076

This paper must be cited as:

The final publication is available at

https://doi.org/10.1016/j.optlaseng.2019.105878

Additional Information

Experimental study of the influence of FBG length on Optical Shape Sensor performance

Ignazio Floris [a,b], Javier Madrigal [a], Salvador Sales [a], Jose M. Adam [b]*,
Pedro A. Calderón [b]

[a]ITEAM , Universitat Politècnica de València, Camino de Vera s/n, Valencia, 46022, Spain
[b]ICITECH, Universitat Politècnica de València, Camino de Vera s/n, Valencia, 46022, Spain

Abstract

This paper compares the performance of optical Multicore Fibres (MCFs) with inscribed Fibre Bragg Gratings (FBGs) used as curvature and shape sensors in relation to strain sensor length. Two fibre optic shape sensors, consisting of FBGs written in standard optical multicore fibre (diameter 124.5 μm), were assembled in the Institute for Telecommunications and Multimedia Applications (iTEAM) of the *Universitat Politècnica de València*. The optical sensors were then positioned on an aluminium mould and quasi-distributed curvature and shape sensing were performed to compare the accuracy of the arrays. It was found that the MCF shape sensor performance strongly depended on FBG length and that sensors based on long FBGs were significantly more accurate, showing that long FBGs can considerably improve shape sensor accuracy at equal grating densities and achieve substantially better performance. This is a great advantage when wavelength division multiplexing is used, when only a limited number of usable FBGs can be applied. These new results, applicable to both multiple single-core optical fibres and multicore optical fibres with embedded quasi-distributed strain sensors, show the connection between strain sensor length and accuracy, hardly taken into account in previous studies, and lay the foundation for the design of new long-FBG-based shape sensors.

Keywords:*Optical Fiber Sensor;Distributed sensing; Multicore Optical Fibre; Bending/Curvature Sensor; Optical Shape Sensing.*

1. Introduction

Fibre Bragg Gratings (FBGs) have been extensively used as strain and temperature sensors[1,2], since they were first proposed in the late 1980s [3]. FBG sensors have many engineering applications [4–9] thanks to their advantages over electric sensors, including: intrinsic safety, multiplexing capabilities, immunity to electromagnetic interference (EMI), resistance to radiation, chemicals and harsh temperatures, light weight and compactness.

Fibre Optic Shape Sensors (FOSS) consist of multiple-core optical cables (a central core and several external cores equally spaced from the sensor axis) with embedded quasi-distributed strain sensors such as FBGs and allow the calculation of local bending (curvature and bending direction) along the fibre based on the strain detected in each core. The 3D fibre shape can thus be reconstructed from the bending parameters [10]. In this way, a cost-effective, compact and monolithic fibre-optic array can be obtained for continuous high-precision 3D shape sensing.

---

38   Curvature and shape sensing by Multicore Fibres (MCFs) are attractive for a number of
39 medical, industrial, civil and defence related applications [11,12]. Villatoro et al. reported on an
40 ultrasensitive bending sensor based on a MCF to monitor the verticality of towers, bridge piles,
41 and buildings [13]. A two-axis temperature-insensitive accelerometer was developed from a
42 multicore FBG bending sensor [14].Westbrook et al. developed a continuous MCF-based shape
43 sensor for distributed sensing applications [15]. Larkin and Shafer filed a patent in 2011 for a
44 completely robotic surgical system through optical fibre bending sensor based on FBGs [16].
45 Moon et al. developed an MCF-based ultrathin shape sensor for minimally invasive surgery [17].
46 MacPherson et al. first demonstrated a multicore fibre displacement sensor with inscribed FBGs
47 for tunnel monitoring [18]. A curvature and shape MCF sensor for continuum robotics was
48 manufactured in 2018 using Draw Tower Gratings (DTG®s) [19]. Khan et al. reported on the
49 development of a shape sensor for flexible medical instruments based on a multicore optical fibre
50 with Bragg gratings [20].
51   This paper reports on an experimental study carried out to identify the influence of FBG length
52 on optical shape sensor performance. Two optical shape sensor arrays were assembled in the
53 Institute of Telecommunications and Multimedia Applications (iTEAM) of the *Universitat*
54 *Politècnica de València* (UPV) by writing 1.5 and 8.0 mm-long Bragg gratings in a standard non-
55 twisted homogeneous 7-core fibre (diameter 124.5 μm) [21]. The sensors were then placed in an
56 aluminium mould and tested by an Optical Spectrum Analyser (OSA) based on Wavelength
57 Division Multiplexing (WDM) analysis.
58   It was found that at the same FBG density the long-FBG-based shape sensor achieved
59 remarkably better accuracy in the entire shape reconstruction process, including strain sensing,
60 curvature calculation and shape integration. Long FBGs can thus notably enhance optical shape
61 sensing accuracy. They are especially useful when FBG density cannot be increased to improve
62 shape reconstruction efficiency, as in WDM analysis, one of the most widely used techniques
63 thanks to their low-cost and high-speed data acquisition, and when the number of usable gratings
64 is limited. However, substituting long FBGs for the short variant can also give better shape
65 reconstruction accuracy in Optical Frequency Domain Reflectometry (OFDR), which can
66 interrogate thousands of gratings [22] with an equal number of strain sensors. Although only
67 multicore fibre sensors were considered, the outcomes are also applicable to optical shape sensors,
68 needles and inclinometers composed of multiple mono-core optical fibres with embedded strain-
69 sensors, which have the same geometry as multicore fibres, but greater core spacing to achieve
70 higher precision [23–27].
71   This paper first demonstrates the relationship between MCF-based shape sensor accuracy and
72 FBG length and then describes the remarkable benefits of strong gratings and hence lays the
73 foundations for the design of more accurate shape sensors.

74 **2. Sensing system and principles**

75 *2.1. Shape sensors fabrication*

76   The shape sensors were assembled in the Institute of Telecommunications and Multimedia
77 Applications (iTEAM) of the Universitat Politècnica de València (UPV) by inscribing four FBGs
78 with a length of 1.5 mm and 8.0 mm (equally spaced along a length of 45mm) in a commercial
79 seven-core MCF from Fibercore Ltd. [21]. The fibre had a cladding diameter of 124.5μm and
80 seven cores with doubly symmetric configuration (see Fig. 1): one central core and six external

81   cores equidistant from the fibre axis (core spacing 35 μm) and 60º of angular spacing. Each core
82   had a mode field diameter of 6.4 μm and a numerical aperture of 0.2.

83
84   **Fig. 1.** Seven- core MCF cross section [21]
85
86   In order to enhance photosensitivity, the fibre optic was hydrogen loaded for two weeks at
87   ambient temperature and a pressure of 20 bars. The phase-mask method [1] was used to inscribe
88   the fibre Bragg gratings by a 244 nm CW frequency-doubled argon-ion laser with 60 mW output
89   power. The spectrum of the central core of both sensors is shown in Fig. 2.
90
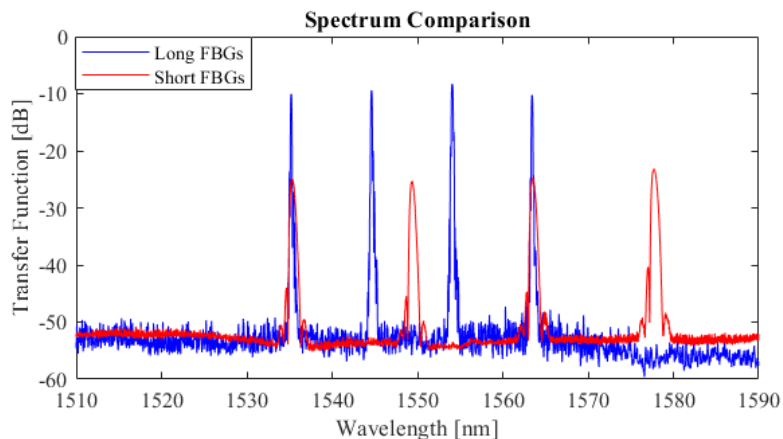
91
92   **Fig. 2.** Spectrum comparison of the two sensors with long and short FBGs.
93

94   *2.2. Shape reconstruction*

95   Optical Fibre Sensors (OFS) with multiple cores and embedded strain sensors have shape
96   reconstruction capabilities. Kirchhoff's rod hypotheses (which state that the cross sections remain
97   plane and normal to the centreline and that the centreline is inextensible [28]) are applicable to the
98   present study (negligible shear deformation) and can be used to define the relationship between the
99   deformed fibre frame and 3D curve frame along the sensor length, when the fibre optic cable is
100   bounded at one extremity in the absence of friction [29].
101   Under the assumptions of the elastic rod theory, the strain varies linearly along each section
102   when the fibre is bent and external torsion/twisting is avoided (there is no local twisting). This
103   torsion/twisting should not be confused with the geometric torsion τ. If twisting cannot be
104   prevented, the torsional strain can be calculated by comparing the strain sensed by the external
105   cores and the central core, where the strain component is zero, and the bending strain can be
106   considered separately [30].

107   In the light of the above, the bending strain function, $\varepsilon(x,y)$, which describes the strain variation
108   due to bending along the section (strain surface), is a plane. The equation of this plane (see Eq.1)
109   can be determined from the coordinates of the cores (after defining a local Cartesian Coordinate
110   System (x,y) centred on the mid-section) and the strains measured by at least three non-aligned
111   cores, although additional cores can be used to obtain higher precision. Moreover, temperature
112   compensation is not necessary, since, thanks to the small core spacing, temperature variations
113   affect all the cores equally (there are no temperature gradients inside the section).
114   The coefficients of the plane can be equated by minimising the Sum of Squared Errors (SSE),
115   as shown in the following Equations [31]:

116    $$\varepsilon(x,y) = a + bx + cy \tag{1}$$

117    $$SSE(a,b,c) = \sum_{i=1}^{n}(\varepsilon_i - a - bx_i - cy_i)^2 \tag{2}$$

118    $$\nabla SSE(a,b,c) = 0 \tag{3}$$

119    $$\begin{cases} \frac{\partial SSE(a,b,c)}{\partial a} = 0 \rightarrow na + b\sum_{i=1}^{n}x_i + c\sum_{i=1}^{n}y_i = \sum_{i=1}^{n}\varepsilon_i \\ \frac{\partial SSE(a,b,c)}{\partial b} = 0 \rightarrow a\sum_{i=1}^{n}x_i + b\sum_{i=1}^{n}x_i^2 + c\sum_{i=1}^{n}x_iy_i = \sum_{i=1}^{n}x_i\varepsilon_i \\ \frac{\partial SSE(a,b,c)}{\partial c} = 0 \rightarrow a\sum_{i=1}^{n}y_i + b\sum_{i=1}^{n}x_iy_i + c\sum_{i=1}^{n}y_i^2 = \sum_{i=1}^{n}y_i\varepsilon_i \end{cases} \tag{4}$$

120   where a, b, and c are the coefficients of the bending strain plane equation, n is the number of
121   cores, x_i, y_i and ε_i are the coordinates and the strain of the ith core.
122
123   The approach described above is valid for a generic MCF section with n cores. In the case of a
124   seven-core fibre, thanks to the doubly symmetry of the section, the system of equations becomes
125   diagonal:

126    $$\begin{cases} na + 0 + 0 = \sum_{i=1}^{n}\varepsilon_i \\ 0 + b\sum_{i=1}^{n}x_i^2 + 0 = \sum_{i=1}^{n}x_i\varepsilon_i \\ 0 + 0 + c\sum_{i=1}^{n}y_i^2 = \sum_{i=1}^{n}y_i\varepsilon_i \end{cases} \tag{5}$$

127   The coefficients of bending strain plane, a, b, and c represent the average longitudinal strain,
128   ε_{long}, and the two components of curvature, κ_x and κ_y, respectively; the latter two being the partial
129   derivatives of $\varepsilon(x,y)$ with respect to x and y. Therefore, the equations become:

130    $$\begin{cases} \varepsilon_{long} = \sum_{i=1}^{n}\varepsilon_i / n \\ \kappa_x = \sum_{i=1}^{n}x_i\varepsilon_i / \sum_{i=1}^{n}x_i^2 \\ \kappa_y = \sum_{i=1}^{n}y_i\varepsilon_i / \sum_{i=1}^{n}y_i^2 \end{cases} \tag{6}$$

131   Once known the coefficients of bending strain function, the bending direction angle, α, and the
132   magnitude of the vector curvature, $|\kappa|$, can be also determined, as shown in Fig. 3, using the
133   following equations:

134    $$|\kappa| = \sqrt{\kappa_x^2 + \kappa_y^2} \tag{7}$$

135    $$\alpha = \tan^{-1}(\kappa_x/\kappa_y) \tag{8}$$

136
137
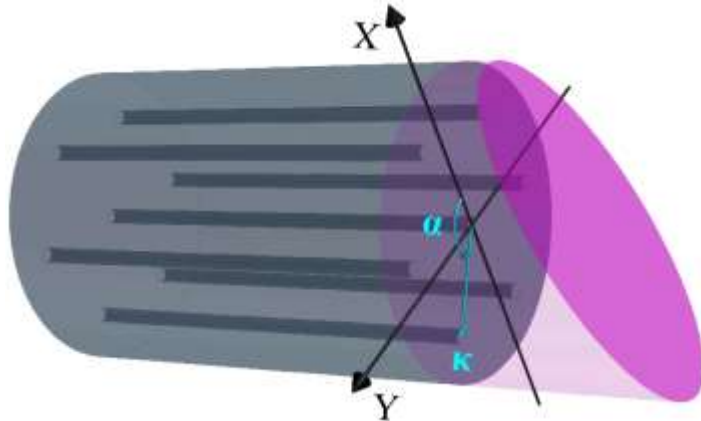138   **Fig. 3.** Strain distribution due to bending of a seven-core fibre

139
140   It is worth noting that the central core does not contribute anything to the bending direction
141   angle and curvature calculations, and thus neither to shape reconstruction, even though it can be
142   used to sense twisting.
143   When the curvature and bending direction angle values are known in several sections, the
144   function of curvature $\kappa(s)$ and torsion $\tau(s)$ along the fibre can be calculated by interpolation or
145   curve fitting [10,32]. Once these functions and the boundary conditions are known, which are the
146   position r_0 and the Frenet frame T_0, N_0, B_0 of the starting point, the shape can be reconstructed
147   through numerical integration of the Frenet-Serret formulas [10], which can be written as:

148    $$\begin{bmatrix} T' \\ N' \\ B' \end{bmatrix} = \begin{bmatrix} 0 & \kappa & 0 \\ -\kappa & 0 & \tau \\ 0 & -\tau & 0 \end{bmatrix} \begin{bmatrix} T \\ N \\ B \end{bmatrix} \tag{9}$$

149   where T, N and B are respectively tangent, normal and binormal vectors.

150
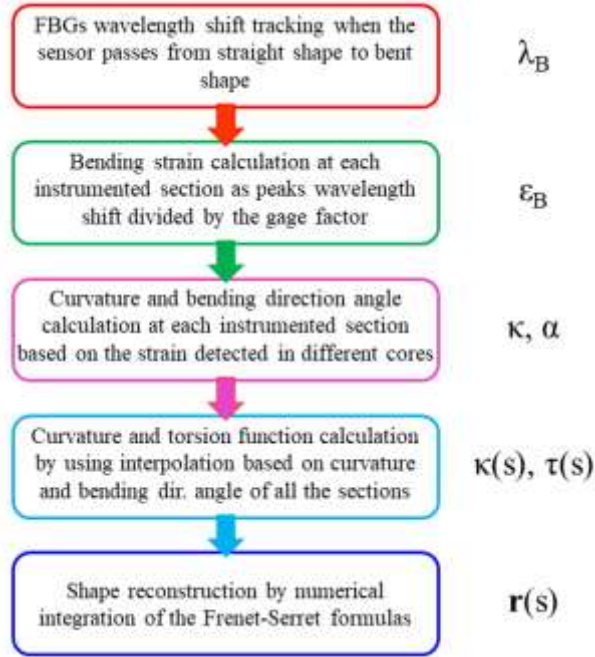151   The flowchart of the whole shape reconstruction process is shown in Fig. 4.
152

157   The torsion function was not calculated in this study, since the fibre was neither spun nor
158 fastened to the mould, and so, as it was impossible to calculate either torsional strain or avoid fibre
159 twisting, 2D shape sensing was used. In this case, the Frenet-Serret formulas become:

160
$$\begin{bmatrix} T' \\ N' \end{bmatrix} = \begin{bmatrix} 0 & \kappa \\ -\kappa & 0 \end{bmatrix} \begin{bmatrix} T \\ N \end{bmatrix} \tag{10}$$

161 *2.3. Experimental setup*

162   In order to test sensor performance, an experimental setup was designed to ensure accurate
163 readings. An aluminium mould was made on a high-precision computer numerical controlled
164 (CNC) machine with a maximum positioning error of a few tens of micrometers to ensure the
165 marginal influence of fibre positioning errors on shape reconstruction accuracy. The mould (see
166 Fig. 5) consisted of a plate with five engraved semicircles with radii of 55, 50, 45, 40 and 35 mm,
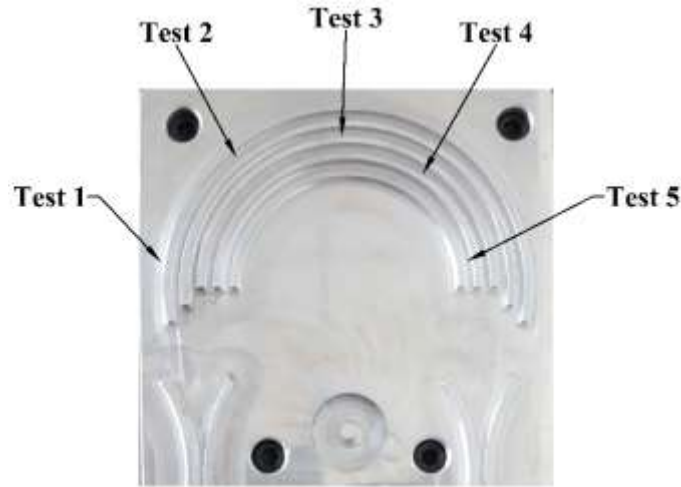167 for Tests1 to 5, respectively.
168

169
170
171
172   **Fig. 5.** Shape-sensing mould
173

174   The fibres were placed around each of the semi-circles on the mould, from the lowest to the
175   highest curvature, and stretched along the semicircles using two multi-axis stages for nano-
176   positioning, interrogated by a Static Optical Sensing Interrogator (sm125) combined with a
177   Channel Multiplexer (sm041) (Micron Optics). The experimental setup can be seen in Fig. 6.
178

179
180
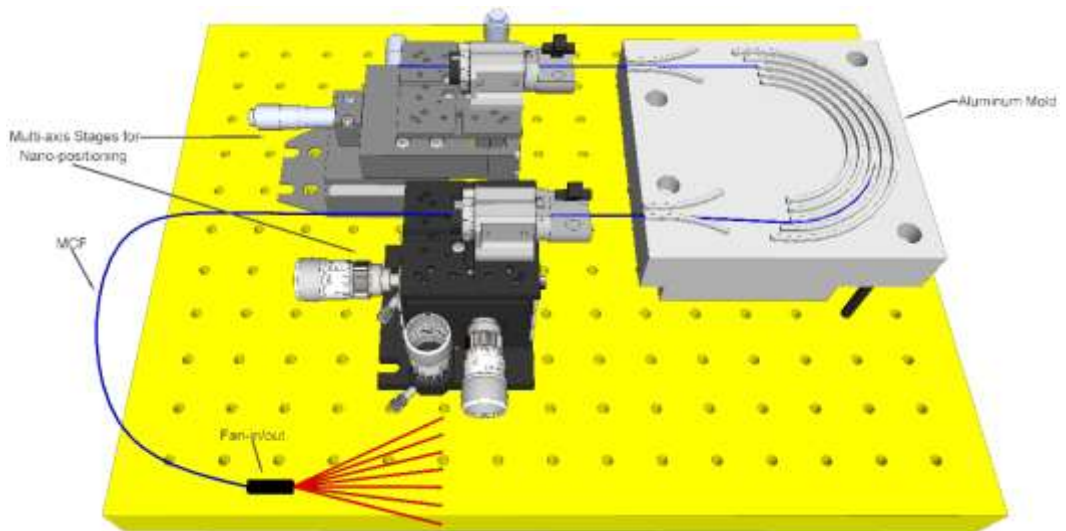181   **Fig. 6.** Experimental setup

182   **3. Results and discussion**

183   *3.1. Strain sensing results*

184   Since the local bending in each instrumented section was calculated from the strain sensed by
185   the cores, the repeatability and precision of the MCF strain sensors were first assessed by tracking

186 the FBG peaks simultaneously in all seven cores at a constant temperature for two minutes at an
187 acquisition rate of 0.5 Hz. The shift in the FBG wavelength was then converted into strain by
188 dividing the wavelength shift by a gauge factor value equal to 1.2 microstrain/pm, obtained from
189 different tensile tests in accordance with [33].
190   The measured strain values followed a normal distribution. Their standard deviations (SD) are
191 reported in Table 1:

192 **Table 1.** Comparison of the normal strain distribution SDs detected by MCF shape sensors.

	Standard Deviation of Strain Measurements [$\mu\varepsilon$] - Test 1							
	Core 1	Core 2	Core 3	Core 4	Core 5	Core 6	Core 7	
FBG 1	0.4911	0.6175	0.5673	0.5437	0.5616	0.6042	0.6095	
FBG 2	0.6126	0.6045	0.5823	0.5400	0.4553	0.4629	0.5776	**Long**
FBG 3	0.4590	0.7009	0.8630	0.6308	0.6439	0.4951	0.5001	**FBGs**
FBG 4	0.5586	0.6590	0.7115	0.6467	0.5339	0.6587	0.5356	
FBG 1	1.7457	2.0023	1.9268	1.6449	1.6916	2.3905	1.7643	
FBG 2	2.3445	1.8208	1.6640	2.5776	1.6821	2.0045	1.8354	**Short**
FBG 3	1.9885	1.6443	2.3988	2.5314	3.0691	1.7810	1.3503	**FBGs**
FBG 4	1.5843	1.5292	2.0616	2.6288	2.2684	2.0137	1.9562	

193
194   The strain distribution SDs were mostly homogeneous in all the sections and cores of both
195 sensors and were strongly affected by grating length. In fact, those of the short FBGs were three
196 or four times higher than those detected by the long FBGs.
197   Strain detection precision depends on the accuracy of the interrogation system, which is related
198 to the resolution of the read-out of the reflected wavelengths, peak tracking technique [34], FBG
199 spectrum and the noise signal.

200 *3.2. Curvature sensing results*

201   Curvature was calculated from the bending strain, which is the difference between the strain
202 measured in the straight and bent sensors. To calculate the bending strain, the FBG wavelength
203 peaks were initially detected in the straight sensors and then the peaks shifts were tracked in the
204 curved fibres. The wavelength peak shifts were converted into strain by dividing them by the
205 gauge factor, while the curvature was calculated from Eqs. 6 and 7.
206   Although the peak shifts are influenced by the longitudinal strain due to axial loading and
207 temperature variation, no compensation was necessary since the longitudinal strain affects all the
208 cores equally and therefore has no influence on the slope of the bending strain plane, on which the
209 curvature depends.
210   Once again, the results of the long-FBG-based MCF are considerably better. The sources of
211 errors in the case of curvature sensing are diverse and include the resolution of the interrogation
212 system and inaccuracy in the geometry of the sensor and in the sensor positioning [31,35,36].
213   Table 2 lists the curvature detected by both sensors in the five tests.
214
215
216
217
218

219   **Table 2.** Comparison of curvature values detected by two MCF shape sensors.

|	*Test 1*	*Test 2*	*Test 3*	*Test 4*	*Test 5*	
Curvature [1/m]	18.1818	20.0000	22.2222	25.0000	28.5714	
Section 1	18.3154	19.7832	22.3003	24.7801	28.3600	
Section 2	17.9226	20.0031	21.9657	25.1781	28.3339	
Section 3	18.5390	19.8496	22.7328	25.3513	28.4611	
Section 4	17.8365	20.0638	22.3428	24.9200	28.5443	**Long FBGs**
Average Value	18.1534	19.9249	22.3354	25.0574	28.4248	
Average Error	-0.0284	-0.0751	0.1132	0.0574	-0.1466	
St. Deviation	0.2867	0.1131	0.2720	0.2217	0.0838	
Section 1	17.8974	19.6786	21.5104	25.4391	28.6197	
Section 2	18.2177	19.8971	21.9127	24.5911	28.6836	
Section 3	18.0101	19.6753	22.5028	25.3401	28.6064	
Section 4	19.1247	21.2615	23.7737	25.7340	30.0321	**Short FBGs**
Average Value	18.3125	20.1281	22.4249	25.2761	28.9854	
Average Error	0.1306	0.1281	0.2027	0.2761	0.4140	
St. Deviation	0.4828	0.6605	0.8550	0.4212	0.6050	

220   *3.3. Shape sensing results*

221   An algorithm was developed in Mathematica code [37] for the linear interpolation of the
222   curvature function $\kappa(s)$, based on the curvature calculated in the instrumented sections, and to
223   reconstruct the 2D shape of the of MCF arrays through numerical integration of the Frenet-Serret
224   equations (Eq. 10). Fig. 7 shows the shapes of the two fibre optic sensors, which were sensed,
225   while the fibres were stretched along the semicircles on the mould (see Fig. 5), and reconstructed
226   by using the procedure explained in Section 2.2.
227
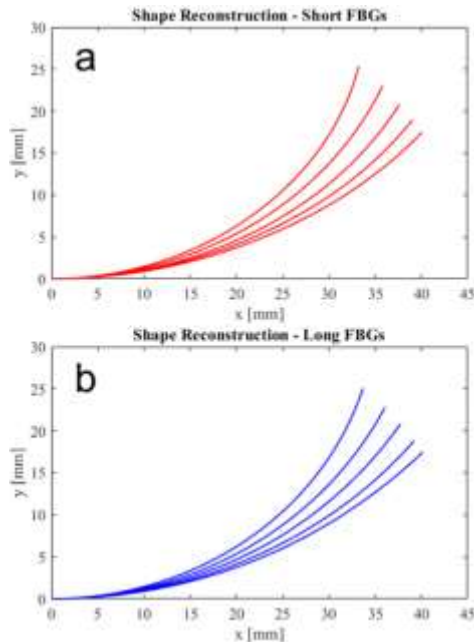
228
229   **Fig. 7.** Reconstructed shape of MCF sensors by (a) short FBGs and (b) long FBGs.

230   In order to evaluate the shape sensors performance, the shape reconstruction errors were
231   determined (considered as the distance between the exact position of the fibres and the
232   reconstructed shape position) (see Fig. 8).
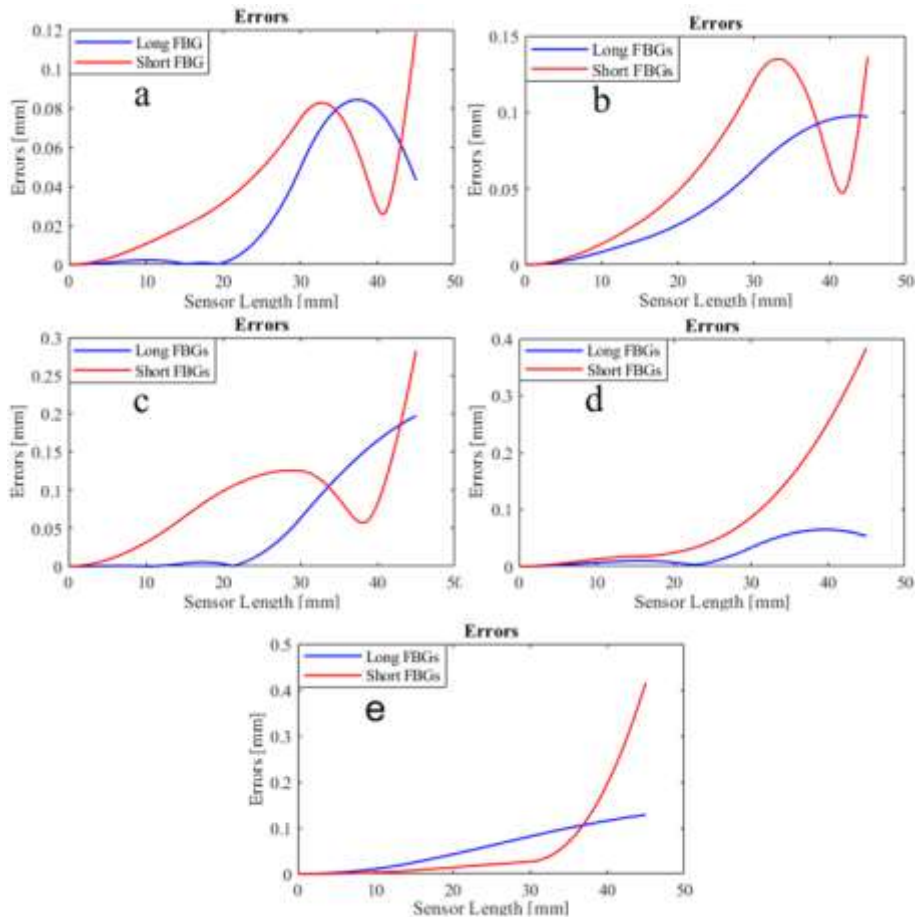
233
234   **Fig. 8.** Shape reconstruction errors of two MCF shape sensor arrays in (a) Test 1; (b) Test 2; (c) Test 3; (d) Test 4; (e)
235   Test 5.
236

237   As in the previous cases, the errors obtained with multicore sensors based on short FBGs are
238   significantly greater, meaning that the strain and curvature sensing errors propagate and affect
239   shape reconstruction, the sources of errors being, in fact, the same discussed in the previous
240   sections. The largest long FBG errors are between 0.05 and 0.20 mm (0.11% and 0.44% of sensor
241   length), while those of the short FBG sensors are several times greater, i.e. between 0.12 and 0.41
242   mm (0.26% and 0.91% of sensor length) and vary much more widely.

243   *3.4. Discussion*

244   The optical MCF sensor based on long FBGs was shown to be significantly more precise and
245   efficient than the short-FBG-based variant. The main reason for the different performance is due
246   to the capacity of long FBGs to average the local errors of longer sections and to the differences in
247   the sensors' spectra (see Fig. 2). Long FBGs are considerably stronger than short ones and so the
248   peaks are narrower and can be detected more efficiently, as can be seen in Fig. 9.
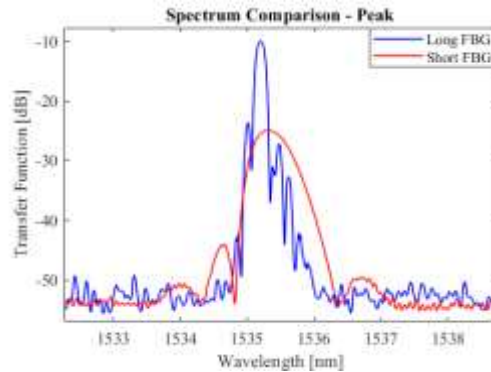
249
250   **Fig. 9.** Peak comparison of long and short FBGs.
251

252   To sum up, long FBGs can improve the accuracy of fibre optic shape sensors without
253   increasing FBG density per metre. This effect is particularly favourable with the WDM technique,
254   because the number of trackable FBGs is limited and cannot be increased to improve shape
255   reconstruction resolution. In addition, WDM analysis is the only one that reaches high frequency
256   data acquisition.

257   **4. Conclusions**

258   Two optical MCF shape sensors were assembled by inscribing long (8.0mm) and short
259   (1.5mm) FBGs in commercial 7-core fibre. All the necessary steps for shape reconstruction were
260   traced, including strain sensing, curvature calculation and shape integration, and sensor
261   performance was compared at each stage.
262   The long-FBG-based sensor was found to be considerably more accurate in all conditions than
263   the short, which was attributed to the capacity of the former to average local errors in longer
264   sections and to its stronger and narrower reflection peaks than those of the short ones, which
265   means the wavelength shift of long FBGs is easier to track.
266   The study first proved that long FBGs can significantly enhance the shape tracking accuracy of
267   optical multicore fibre sensors. When wavelength division multiplexing is employed and the
268   number of usable FBGs is limited and depends on the breadth of the spectral transmission
269   window, long gratings are especially recommended since they can considerably improve precision
270   with the same number of gratings. Nevertheless, even when the FBGs are interrogated by an
271   OFDR, which allows higher grating density by reading up to several thousand gratings, long
272   gratings can still ensure better performance at equal FBG densities. The results obtained apply to
273   both multiple single-core optical fibres and multicore optical fibres with embedded quasi-
274   distributed strain sensors, which have the same cross section geometry. In the light of the above,
275   these new results lay the basis for the design of new and more efficient shape sensors.

Acknowledgments

References

[1]   Kashyap R. Fiber Bragg Gratings. 2nd Editio. Elsevier; 2009.

[2]   Zhang S, Bae Lee S, Fang X, Sam Choi S. In-fiber grating sensors. Opt Lasers Eng 1999;32:405–18. doi:10.1016/S0143-8166(99)00052-4.

[3]   Meltz G, Dunphy JR, Glenn WH, Farina JD, Leonberger FJ. Fiber Optic Temperature And Strain Sensors. In: Verga Scheggi AM, editor., 1987, p. 104. doi:10.1117/12.941093.

[4]   Rao Y. Recent progress in applications of in-fibre Bragg grating sensors. Opt Lasers Eng 1999;31:297–324. doi:10.1016/S0143-8166(99)00025-1.

[5]   Campanella C, Cuccovillo A, Campanella C, Yurt A, Passaro V. Fibre Bragg Grating Based Strain Sensors: Review of Technology and Applications. Sensors 2018;18:3115. doi:10.3390/s18093115.

[6]   Ferraro P, De Natale G. On the possible use of optical fiber Bragg gratings as strain sensors for geodynamical monitoring. Opt Lasers Eng 2002;37:115–30. doi:10.1016/S0143-8166(01)00141-5.

[7]   Spirin V., Shlyagin M., Miridonov S., Jiménez FJM, Gutiérrez RML. Fiber Bragg grating sensor for petroleum hydrocarbon leak detection. Opt Lasers Eng 1999;32:497–503. doi:10.1016/S0143-8166(00)00021-X.

[8]   Botsis J, Humbert L, Colpo F, Giaccari P. Embedded fiber Bragg grating sensor for internal strain measurements in polymeric materials. Opt Lasers Eng 2005;43:491–510. doi:10.1016/j.optlaseng.2004.04.009.

[9]   Ma Z, Chen X. Fiber Bragg Gratings Sensors for Aircraft Wing Shape Measurement: Recent Applications and Technical Analysis. Sensors 2018;19:55. doi:10.3390/s19010055.

[10]   Moore JP, Rogge MD. Shape sensing using multi-core fiber optic cable and parametric curve solutions. Opt Express 2012;20:2967. doi:10.1364/OE.20.002967.

[11]   Amanzadeh M, Aminossadati SM, Kizil MS, Rakić AD. Recent developments in fibre optic shape sensing. Meas J Int Meas Confed 2018;128:119–37. doi:10.1016/j.measurement.2018.06.034.

[12]   Wang Q, Liu Y. Review of optical fiber bending/curvature sensor. Meas J Int Meas Confed 2018;130:161–76. doi:10.1016/j.measurement.2018.07.068.

[13]   Villatoro J, Van Newkirk A, Antonio-Lopez E, Zubia J, Schülzgen A, Amezcua-Correa R. Ultrasensitive vector bending sensor based on multicore optical fiber. Opt Lett 2016;41:832–5. doi:10.1364/OL.41.000832.

[14]   Fender A, MacPherson WN, Maier RRJ, Barton JS, George DS, Howden RI, et al. Two-axis accelerometer based on multicore fibre Bragg gratings. IEEE Sens J 2007;8:66190Q-66190Q – 4. doi:10.1117/12.738411.

[15]   Westbrook PS, Kremp T, Feder KS, Ko W, Monberg EM, Wu H, et al. Continuous Multicore Optical Fiber Grating Arrays for Distributed Sensing Applications. J Light Technol 2017;35:1248–52. doi:10.1109/JLT.2017.2661680.

[16]   Larkin DQ, Shafer DC. Robotic surgery system including position sensors using fiber bragg gratings. US7930065B2, 2011.

[17]   Moon H, Jeong J, Kang S, Kim K, Song Y-W, Kim J. Fiber-Bragg-grating-based ultrathin shape sensors displaying single-channel sweeping for minimally invasive surgery. Opt Lasers Eng 2014;59:50–5. doi:10.1016/j.optlaseng.2014.03.005.

[18]   MacPherson WN, Silva-Lopez M, Barton JS, Moore AJ, Jones JDC, Zhao D, et al. Tunnel monitoring using multicore fibre displacement sensor. Meas Sci Technol 2006;17:1180–5. doi:10.1088/0957-0233/17/5/S41.

[19]   Jan VR, Vincent M, Eric L, Bram VH, Christian V, Johan V, et al. Curvature and Shape Sensing for Continuum Robotics using Draw Tower Gratings in Multi Core Fiber. 26th Int. Conf. Opt. Fiber Sensors, Washington, D.C.:

321   OSA; 2018, p. ThE70. doi:10.1364/OFS.2018.ThE70.

322   [20]   Khan F, Denasi A, Barrera D, Madrigal J, Sales S, Misra S. Multi-core Optical Fibers with Bragg Gratings as

323   Shape Sensor for Flexible Medical Instruments. IEEE Sens J 2019;PP:1–1. doi:10.1109/JSEN.2019.2905010.

324   [21]   https://www.fibercore.com/product/multicore-fiber n.d.

325   [22]   Childers BA, Froggatt ME, Allison SG, Moore, Sr. TC, Hare DA, Batten CF, et al. Use of 3000 Bragg grating

326   strain sensors distributed on four eight-meter optical. In: McGowan A-MR, editor., 2001, p. 133–42.

327   doi:10.1117/12.429650.

328   [23]   Lenke P, Wendt M, Krebber K, Glötzl R. Highly sensitive fiber optic inclinometer: easy to transport and easy to

329   install. 21st Int. Conf. Opt. Fibre Sensors, vol. 7753, 2011, p. 775352. doi:10.1117/12.884695.

330   [24]   Wang YL, Shi B, Zhang TL, Zhu HH, Jie Q, Sun Q. Introduction to an FBG-based inclinometer and its

331   application to landslide monitoring. J Civ Struct Heal Monit 2015;5:645–53. doi:10.1007/s13349-015-0129-4.

332   [25]   Bang H-J, Kim H-I, Lee K-S. Measurement of strain and bending deflection of a wind turbine tower using

333   arrayed FBG sensors. Int J Precis Eng Manuf 2012;13:2121–6. doi:10.1007/s12541-012-0281-2.

334   [26]   Park Y, Elayaperumal S, Daniel B, Ryu SC, Shin M, Savall J, et al. Real-Time Estimation of 3-D Needle Shape

335   and Deflection for MRI-Guided Interventions. IEEE/ASME Trans Mechatronics 2010;15:906–15.

336   doi:10.1109/TMECH.2010.2080360.

337   [27]   Roesthuis RJ, Kemp M, van den Dobbelsteen JJ, Misra S. Three-Dimensional Needle Shape Reconstruction

338   Using an Array of Fiber Bragg Grating Sensors. IEEE/ASME Trans Mechatronics 2014;19:1115–26.

339   doi:10.1109/TMECH.2013.2269836.

340   [28]   O'Reilly OM. Kirchhoff's Rod Theory. Model. Nonlinear Probl. Mech. Strings Rods Role Balanc. Laws, Cham:

341   Springer International Publishing; 2017, p. 187–268. doi:10.1007/978-3-319-50598-5_5.

342   [29]   Langer J, Singer D a. Lagrangian Aspects of the Kirchhoff Elastic Rod. SIAM Rev 1996;38:605–18.

343   doi:10.1137/S0036144593253290.

344   [30]   Askins CG, Miller GA, Friebele EJ. Bend and Twist Sensing in a Multiple-Core Optical Fiber. OFC/NFOEC

345   2008 - 2008 Conf. Opt. Fiber Commun. Fiber Opt. Eng. Conf., IEEE; 2008, p. 1–3.

346   doi:10.1109/OFC.2008.4528404.

347   [31]   Floris I, Calderón PA, Sales S, Adam JM. Effects of core position uncertainty on optical shape sensor accuracy.

348   Meas J Int Meas Confed 2019;139. doi:10.1016/j.measurement.2019.03.031.

349   [32]   Jäckle S, Strehlow J, Heldmann S. Shape Sensing with Fiber Bragg Grating Sensors. In: Handels H, Deserno

350   TM, Maier A, Maier-Hein KH, Palm C, Tolxdorff T, editors. Bild. für die Medizin 2019, Wiesbaden: Springer

351   Fachmedien Wiesbaden; 2019, p. 258–63. doi:10.1007/978-3-658-25326-4_58.

352   [33]   Black RJ, Zare D, Oblea L, Park Y-L, Moslehi B, Neslen C. On the Gage Factor for Optical Fiber Grating Strain

353   Gages. Proc Soc Adv Mater Process Eng 2008;52, 2008.

354   [34]   Tosi D. Review and Analysis of Peak Tracking Techniques for Fiber Bragg Grating Sensors. Sensors

355   2017;17:2368. doi:10.3390/s17102368.

356   [35]   Floris I, Sales S, Calderón PA, Adam JM. Measurement uncertainty of multicore optical fiber sensors used to

357   sense curvature and bending direction. Meas J Int Meas Confed 2019;132.

358   doi:10.1016/j.measurement.2018.09.033.

359   [36]   Henken KR, Dankelman J, Van Den Dobbelsteen JJ, Cheng LK, Van Der Heiden MS. Error Analysis of FBG-

360   Based Shape Sensors for Medical Needle Tracking. IEEE/ASME Trans Mechatronics 2014;19:1523–31.

361   doi:10.1109/TMECH.2013.2287764.

362   [37]   Wolfram S. The Mathematica Book, Fifth Edition. Wolfram Media, Inc; 2003.

363